Received: 23 February 2021 | Accepted: 16 August 2021

DOI: 10.1111/2041-210X.13709

Methods in Ecology and Evolution BRITISH ECOLOGICAL SOCIETY

RESEARCH ARTICLE

Terrestrial laser scanning to reconstruct branch architecture from harvested branches

Phil Wilkes[1,2] | **Alexander Shenkin**[3] | **Mathias Disney**[1,2] | **Yadvinder Malhi**[3] | **Lisa Patrick Bentley**[4] | **Matheus Boni Vicari**[1]

[1]Department of Geography, University College London, London, UK

[2]NERC National Centre for Earth Observation, Leicester, UK

[3]Environmental Change Institute, School of Geography and Environment, University of Oxford, Oxford, UK

[4]Department of Biology, Sonoma State University, Rohnert Park, CA, USA

Correspondence
Phil Wilkes
Email: p.wilkes@ucl.ac.uk

Funding information
Natural Environment Research Council, Grant/Award Number: NE/P011780/1

Handling Editor: Carlos Alberto Silva

Abstract

1. Quantifying whole branch architecture is critical to understanding tree function, for example, branch surface area controls woody gas exchange. Yet, due to measurement difficulty, branch architecture of small diameter branches (e.g. <10 cm ∅) is modelled, subsampled or ignored. Methods that use terrestrial laser scanning (TLS) are now being widely applied to analyse tree and plot-level tree architecture; however, resolving small diameter branches in-situ remains a challenge.
2. Currently, it is suggested that accurate reconstruction of small diameter branches can only be achieved by harvest and measurement in controlled conditions. Here we present a new TLS workflow for rapid and accurate reconstruction of complete branch architecture from harvested branches. The workflow sets out scan configuration, post-processing (including a novel reflectance filter) and fitting of quantitative structure models (QSM) to reconstruct topologically coherent branch models. This is demonstrated on 595 branches (scanned indoors to negate the impact of wind) and compared with 65 branches that were manually measured (i.e. with measuring tape and callipers).
3. Comparison of a suite of morphological and topological traits reveals a good agreement between TLS-derived metrics and manual measurements where RMSE (%RMSE) for total branch length = 0.7 m (10%), volume = 0.09 L (43%), surface area = 0.04 m^2 (26%) and *N* tips = 6.4 (35%). Scanning was faster and invariant to branch size compared with manual measurements which required significantly more personnel time. We recommend measuring a subsample of tip widths to constrain the QSM taper function as the TLS workflow tends to overestimate tip width.
4. The workflow presented here allows for a rapid characterisation of branch architecture from harvested branches. Increasing the number of branches analysed (e.g. many branches from a single tree or branches from many species globally) could allow for a comprehensive analysis of the 'missing link' between the leaves and larger diameter branches.

KEYWORDS
architecture, branch, canopy, LiDAR, quantitative structure models, reconstruction, structure, terrestrial laser scanning

1 | INTRODUCTION

Tree architecture is the 3D spatial arrangement, morphology and topology of a tree's leaves, branches and stem (Barthélémy & Caraglio, 2007; Valladares & Lo Niinemets, 2007). An individual tree's architecture is the product of its encoded genome during ontogeny, resulting from both evolutionary and ecological trade-offs between light capture, water transportation and mechanical self-support. Tree architecture is typically measured manually, for example, with a measuring tape and callipers, either in-situ (Sillett et al., 2015) or after destructive harvest (Bentley et al., 2013; MacFarlane & Kane, 2017; Smith et al., 2014); both are laborious, time-consuming and sometimes dangerous tasks (Smith et al., 2014). In particular, characterising the architecture of small diameter woody components is difficult given their often non-trivial complexity and in-situ location many metres above the forest floor. This has resulted in traits of higher-order branching being modelled, subsampled or ignored (Lau et al., 2018; Sillett et al., 2015). Capturing and quantifying the architecture of the 'missing link' between larger diameter branches and leaves is key to understanding whole tree function, for example, gas exchange and surface area allometry (Chambers et al., 2004), intra-canopy response to light environments (Barthélémy & Caraglio, 2007) or divergence from theoretical predictions of crown architecture (Bentley et al., 2013).

Sensor-based methods to capture 3D information of smaller objects (i.e. centimetre to decimetre scale) have been developed for a number of disciplines, including agronomy, ecology, industry, cultural heritage, medicine and criminal investigation (Calders et al., 2019; Rahman et al., 2017; Sansoni et al., 2009). Capturing complex 3D plant structure has been demonstrated using techniques such as stereo vision, structure from motion (SfM) (Iglhaut et al., 2019; Moriondo et al., 2016), structured light (Nguyen et al., 2015) and X-ray tomography (Dutagaci et al., 2020). These techniques allow for a larger sample size without the need for subsampling (i.e. whole branch architecture) and can generate a suite of quantitative measurements. However, these techniques often require controlled laboratory or photo studio conditions and/or large pieces of specialist equipment that make them less ideal for capturing data in remote areas, such as forests.

Terrestrial laser scanning (TLS) methods have also shown great promise for capturing tree and branch architecture (Disney, 2019; Malhi et al., 2018). TLS instruments use a laser range finder to measure the distance along with azimuth and zenith angles of an intercepting surface, for example, ground, wood and leaf, in relation to the instrument. Scanning across a panorama or hemisphere, TLS instruments can quickly construct a dense 3D representation (i.e. a point cloud) of an area of interest. TLS methods have been used to measure tree and forest biophysical traits, including volume and biomass (Calders et al., 2015), branching topology and scaling exponents (Lau et al., 2018, 2019; Martin-Ducup et al., 2020), leaf-level traits (Boni Vicari et al., 2019) and many others (see review by Calders et al., 2020).

However, using TLS to measure small diameter branching architecture (e.g. <10 cm ⌀; Lau et al., 2019; Martin-Ducup et al., 2020) of a tree in-situ still remains a challenge, particularly for large trees or in dense evergreen forests, that is, the tropics. Factors including occlusion, laser beam divergence, wind effects, liana infestation and under sampling preclude accurate characterisation, particularly towards the top of the canopy (Wilkes et al., 2017). This, in turn, can lead to a miss-characterisation of branch architecture as adjacent branches are either aggregated or ignored. When Lau et al. (2019) compared scanned and manually measured branches, TLS methods were only able to reconstruct 56% of branches with a radius of 5–15 cm. In all but the most ideal circumstance, for example, isolated, low stature trees (Calders et al., 2015; Raumonen et al., 2013) and branch harvesting, remains the only viable option.

The capability of TLS methods to accurately scan and reconstruct harvested branches has been tested previously. For example, Cheng et al. (2007) scanned branches from a single position using computer vision techniques to derive branch topology; Keightley and Bawden (2010) mounted grapevines on a rotating platform to capture scans from different viewpoints with the aim of reconstructing volume and del Campo-Sanchez et al. (2019) scanned grapevines in-situ again to estimate volume as a proxy for vigour. Presented here is a scanning and post-processing workflow that is rapid, scalable, transportable to remote areas and is capable of reconstructing whole branch architecture to the branch tip. In all, 595 branches were scanned and reconstructed using this method; the full architecture of 65 branches were measured manually and analogue metrics were compared.

2 | MATERIALS AND METHODS

2.1 | Locations

Branches were harvested from 12 forest plots in Malaysian Borneo, Queensland, Australia and Mato Grosso, Brazil between July 2018 and August 2019 (Table 1). All plots are located in the tropics and cover a range of forest types from savanna (*Cerrado*) to upland rainforest. The Malaysian and Brazilian plots are part of the Global Ecosystem Monitoring (GEM) network (Malhi et al., 2021) and the

TABLE 1 Description of plots and number of branches measured. Country codes are Australia (AUS), Brazil (BRA) and Malaysia (MAL). Pole refers to either a pole-lopper or a pole with a snagging hook, B&A refers to a bow and arrow. 'Full' refers to complete manual measurement of branch architecture whereas 'Tips' refers to measurement of a subsample ($N = 5$) of tip-widths, see Section 2.5 for more details

Plot	Country	Forest type	Harvest method	Scanned	Manually measured	
					Full	Tips
AEP02	AUS	Complex Notophyll Vine Forest	B&A or pole	18	0	15
BEK01	AUS	Upland rainforest refugia	B&A or pole	14	0	12
CBN02	MAL	Tropical rain forest	Climber	32	19	0
CRP01	BRA	*Cerradão*	Pole	9	1	7
CRP02	BRA	*Cerradão*	Pole	12	0	9
DRO01	AUS	Complex Notophyll Vine Forest	Canopy Crane	84	0	72
MLA01	MAL	Tropical rain forest	Climber	78	18	0
NXV01	BRA	*Cerrado tipico*	Pole	113	2	77
NXV02	BRA	*Cerrado rupestre*	Pole	61	3	50
SAF03	MAL	Tropical rain forest; moderately logged	Climber	104	31	0
SAF05	MAL	Tropical rain forest; heavily logged	Climber	20	21	0
VCR02	BRA	Semi-deciduous forest	Pole	50	4	24

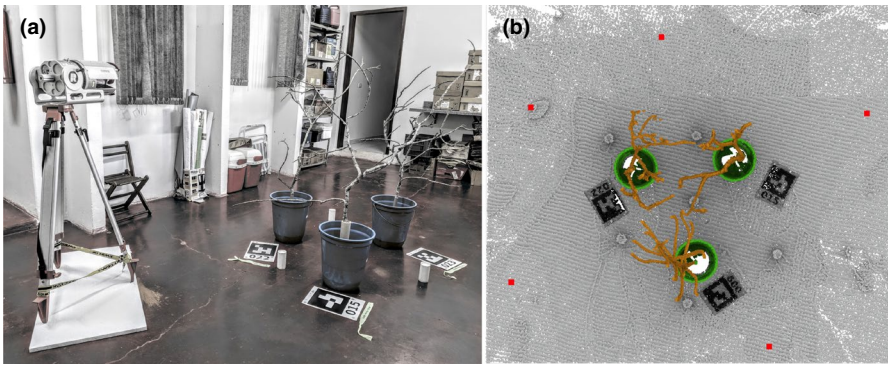

FIGURE 1 Scan set up used for the Nova Xavantina campaign, Brazil (July 2019). (a) the scanner and branches in position, (b) a plan view of a point cloud where the branches (brown), buckets (green) and fiducial markers (grey) are visible, red dots indicate the location of scan positions

Australian plots are part of the CSIRO Rainforest Permanent Plots of North Queensland (Graham, 2006).

2.2 | Branch harvesting and processing

Trees were selected using the protocol described by Shenkin, Bentley, et al. (2020) where species that contributed maximally to plot basal area were selected (up to 80%), then for each identified species three to five individuals were sampled. The aim was to collect a minimum of two branches per tree: a branch from the sunlit part of the canopy and another from a shaded region (immediately below the sunlit canopy). Branches were harvested using a variety of techniques dependent on forest type and personnel (Table 1). The size of harvested branches was determined by the harvesting method and the size of the tree. Ideally branches had a length of >1 m and included >2 branch furcations. Harvested branches were stripped of all leaves, flowers and fruits before measurement.

2.3 | Laser scanning

2.3.1 | Scanner and branch setup

A RIEGL VZ-400 terrestrial laser scanner (RIEGL Laser Measurement Systems GmbH) was used for all scans. In all, 1–6 branches (dependent on branch size) were arranged in a group, orientated so that they would not touch each other or the ground, and scanned simultaneously (Figure 1). Branches were secured in the end of metal tubing and placed in buckets of sand to minimise movement. Fiducial markers (akin to QR codes) were placed on the floor to allow identification of each branch in post-processing (Wilkes, 2021). The markers include a pattern of four retroreflective stickers (10 mm ⌀) which were used to co-register scans.

Between four and six scan positions (collectively known as a project), located around the branches (Figure 1b), were used to capture each set of branches. At each position, a single scan was performed where the scanner rotation axis was approximately perpendicular to the ground plane. A $100^{\circ} \times 80^{\circ}$ field of view was captured at an

angular resolution of 0.02°; each scan took 2:45 min where ~20M laser pulses were fired. The VZ-400 beam has an exit diameter of 0.007 m and a beam divergence of 0.35 mrad; branches were at a maximum distance of 5 m from the scanner, and at this distance maximum cross-sectional beam diameter is ~0.01 m.

The scanning area needed to be large enough to allow easy movement around the branches and minimum distance between the scanner and target (for the RIEGL VZ-400, this is 0.5 m). It should be noted, owing to the restricted scanning field of view, large or featureless areas required additional 'features' (e.g. furniture in the scanning field of view) to assist with registration. Initially, scanning was performed outside but it became clear that branch tips would oscillate even with very low wind speeds; therefore, scanning was moved to an indoor space.

2.3.2 | Co-registration of scan projects

Co-registration of scans in a project is a two-step process (coarse- and fine-registration) that produces a 4 × 4 roto-transformation matrix for each scan position. When applied, a scan is rotated into a common, arbitrary coordinate system (nominally referenced to the first scan position). Co-registration of a project was done using RiSCAN Pro (version 2.5.1; RIEGL Laser Measurement Systems GmbH). Coarse registration was achieved using the retro-reflective stickers on the corners of the fiducial markers. Fine registration was computed using RiSCAN Pro's Multi-Station Adjustment (MSA) method (RIEGL Laser Measurement Systems GmbH, 2019). MSA fits a set of planes to a point cloud by iteratively voxelising the point cloud, with each iteration voxel edge length decreases until plane fit error is below a specified threshold (or no plane is fit if voxel edge of minimum number of point thresholds are exceeded). Here voxel edge length decreased from 1.024 to 0.064 m, minimum points were 10 and maximum plane error was 0.006 m; this resulted in 7,000–20,000 planes per scan position. MSA then uses a least square solution to iteratively adjust scan position to minimise positional error between overlapping planes.

Combining all rotated point clouds produces a single point cloud $\mathscr{P}' = \{\mathbf{p}_0, \ldots, \mathbf{p}_{|\mathscr{P}'|}\}$ where the attributes of each point $\mathbf{p}$ are a vertex in $\mathbb{R}^3$, range corrected relative reflectance ϕ (dB) (RIEGL Laser Measurement Systems GmbH, 2012), deviation d (–), range R (m) and scan position sp. Individual branch point clouds $\mathscr{B}'$ were identified in $\mathscr{P}'$ using the fiducial markers, automatically clipped from $\mathscr{P}'$ and then visually checked for errors, for example, movement of branches between scans.

2.4 | Post-processing

2.4.1 | Filtering points

Terrestrial laser scanning data invariably contain points that are erroneous or is not required, that is, $\mathscr{B}' = \mathscr{B} + \epsilon$ where $\mathscr{B}$ is the branch point cloud and ϵ is to be filtered. There are a number of sources of ϵ, for example, neighbouring objects that were not correctly clipped, that may have to be rectified manually. Two sources of ϵ that required an analytical approach to filter were:

Source 1 errors were filtered using the 'deviation' field so that $\forall \mathbf{p} \in \mathscr{B}' : \mathbf{p}_d \leq 10$. Deviation, a unitless metric, compares the area under the curve of the reflected pulse with that of the expected system response (RIEGL Laser Measurement Systems GmbH, 2012). Low values of $\mathbf{p}_d$ indicate that the reflected pulse shape is similar to the system pulse, larger $\mathbf{p}_d$ values can be caused by ranging errors, for example, where two or more surfaces in the path of the laser pulse are insufficiently separated in space, or by a high incidence angle (Abegg et al., 2020; RIEGL Laser Measurement Systems GmbH, 2012).

Source 2 errors are caused when the beam footprint intersects a surface but the beam centroid does not. If reflected amplitude is large enough, a return will be registered where the centroid of the point is not on the surface of the intercepting object. This can lead to branch radius inflation or topological errors if these points are included in reconstruction (see Section 2.4.2), and it is therefore necessary to filter these points.

To determine whether the centroid of an outgoing laser pulse intercepts a branch, a simple physical model was developed. The model is convolution of a laser footprint F and a cross-section of a branch G. A laser footprint can be defined as a Gaussian F^*

$$F^*(x) = \frac{1}{\sigma\sqrt{2\pi}} e^{-(x-\mu)^2/2\sigma^2}, \tag{1}$$

where μ is the centroid of the footprint and σ is the standard deviation. The effective laser footprint cross-sectional area was determined by constraining F^* to $1/e^2$; therefore, the integral of F is

$$F(x) = \int_{-1/e^2}^{1/e^2} F^*(x)\mathrm{d}x. \tag{2}$$

The branch model G is represented by a cylinder with axis centred on zero and infinite length. It is approximated from Figure 2 that a branch is a Lambertian scatter where reflectance decreases with increasing incidence angle. Therefore, G can be modelled using Lambert's cosine law, where reflectance is proportional to the cosine of the incidence angle and the surface normal.

$$G(-\pi < x < \pi) = \cos(x)R, \tag{3}$$

where R is the radius of the modelled branch.

The convolution of F and G is calculated to compute reflectance, this is then transformed to give ϕ in units of dB.

$$\phi = 10\log_{10}(F \times G), \tag{4}$$

where F and G do not overlap $\phi = -$ and $\phi \to 0$ when $F_\mu = 0$ (Figure 3).

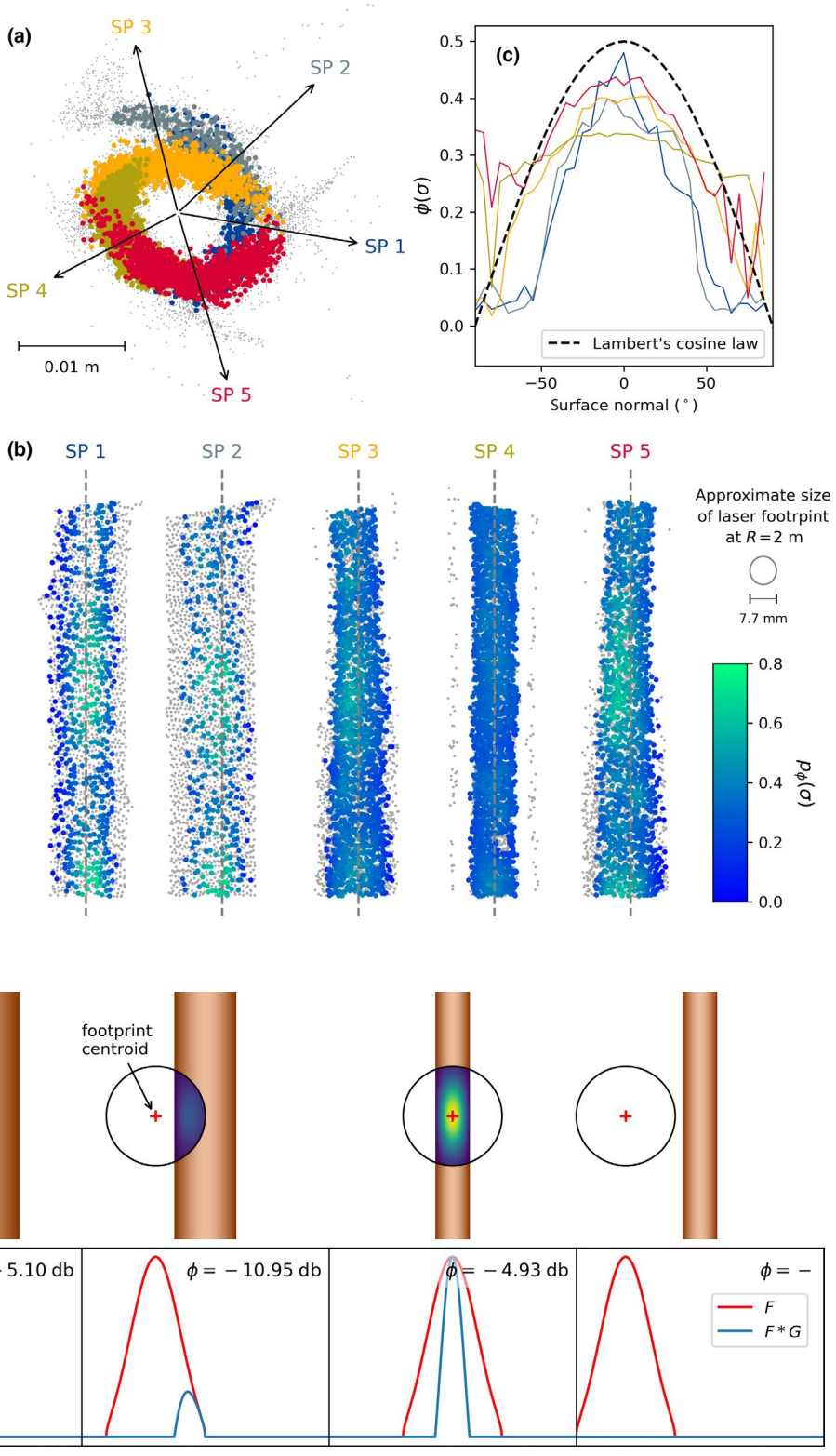

FIGURE 2 Point reflectance for a branch cross-section. (a) a cross-section of a branch section where points are coloured by scan position (SP 1–5) or if they are filtered (grey), (b) point clouds coloured by reflectance (grey points were filtered) where points clouds have been rotated towards the scanner (grey dashed line approximate branch axis) and (c) mean reflectance as a function of surface normal (coloured by scan position; see panel (a)) where normals have been calculated from a local neighbourhood of points, also include is curve representing Lambert's Cosine Law

FIGURE 3 Examples of modelled reflectance with different size branches and footprint locations

Using the model, expected minimum reflectance $E[\phi_{min}]$ as a function of observed maximum reflectance ϕ_{max} was computed (Figure 4). A third-order polynomial was used to model $E[\phi_{min}] / \phi_{max}$ as function of ϕ_{max} (Figure 4b). Particularly towards the ends of branches, too few points may remain after filtering $\mathbf{p}_{\sigma} > E[\phi_{min}]$ to form a cylinder (see Section 2.4.2); therefore, $E[\phi_{min}]$ was multiplied by a factor of 0.8. As an example, if $\phi_{max} = -10$ dB, then $E[\phi_{min}] = -11.04$ dB; therefore, $\forall \mathbf{p}_i \in \mathscr{B}' : \mathbf{p}_{\phi} > -11.04$ dB.

As surface scattering characteristics are likely to differ along a branch, $\mathscr{B}'$ is first voxelised with a voxel length of 0.01 m.

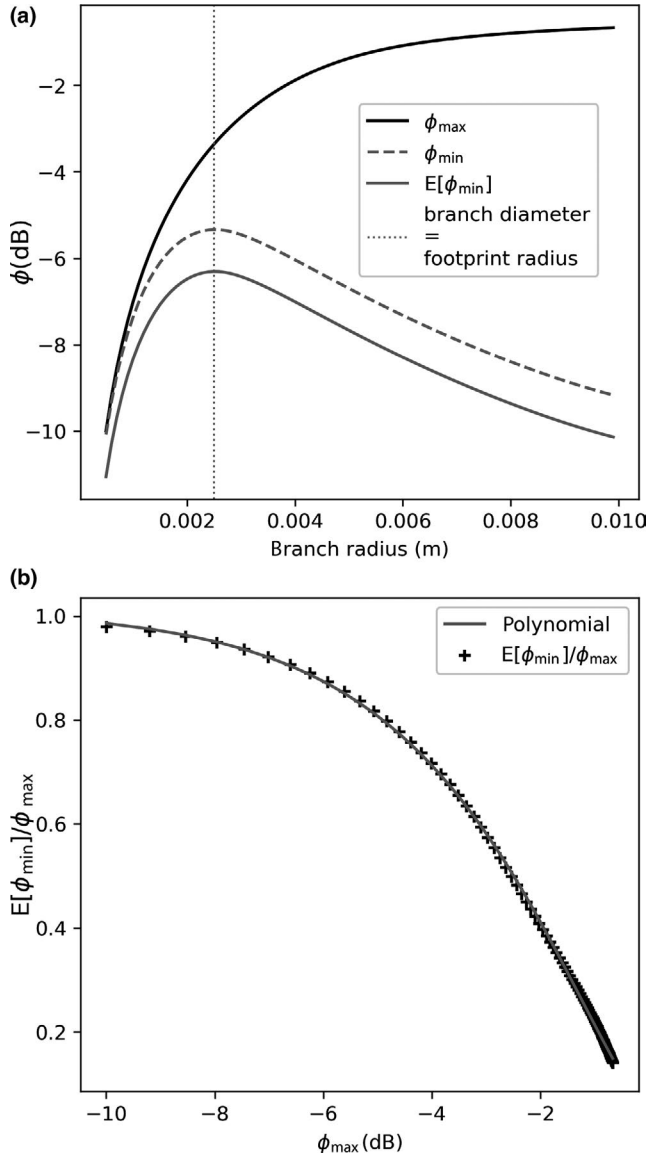

FIGURE 4 Modelled reflectance for a laser footprint with 0.01 m ∅ at ~6 m from a branch with diameter ranging from 0.001 to 0.02 m, (a) modelled ϕ_{max} and E[ϕ_{min}] reflectance and (b) polynomial model fit to E[ϕ_{min}]/ϕ_{max}

Furthermore, as different scan positions have a different viewing geometry of a certain voxel, ϕ_{max} and E[ϕ_{min}] are calculated for each scan position *sp* for each voxel *v*.

$$\phi_{max}(v, sp) = max_{\mathbf{p}\in\mathscr{B}'_{v,sp}} \mathbf{p}_{\phi}. \quad (5)$$

Finally, a nearest neighbour analysis was conducted to remove spatial outliers which were generally artefacts from filtering processes described above. Mean Euclidean distance to the 10 closest neighbouring points $\mathbf{p}_N$ was computed. Points where $\mathbf{p}_N > \mathscr{B}_{N\mu} + \mathscr{B}_{N\sigma}$ were filtered where $\mathscr{B}_{N\mu}$ and $\mathscr{B}_{N\sigma}$ are population mean and standard deviation distances, respectively. Examples of $\mathscr{B}'$ and $\mathscr{B}$ are presented in Figure 5.

2.4.2 | Quantitative structure models

Methods to parameterise unordered points include fitting a plane to or enclosing points in a geometric primitive (e.g. a cylinder), this allows computation of a surface normal or volume, respectively (Disney et al., 2018). In the case of tree point clouds, methods have been developed to segment $\mathscr{P}$ into a set of spatially separate clusters $\mathscr{C} = \{c_i, \ldots, c_N\}$, where *N* is the number of clusters; each c_i are then enclosed with a cylinder. A graph can then be constructed from $\mathscr{C}$ to connect all cylinders into a topologically coherent network. The cylinder representation and topology are more commonly known as a Quantitative Structure Model or QSM. QSMs allow the grouping of cylinders into internodes, that is, lengths of branch between two furcations, determination of internode parent–child relationships, estimation of path length and many other attributes (Raumonen et al., 2013).

The *treegraph* software (Boni Vicari & Wilkes, 2021) was used to generate QSMs for each branch to parameterise $\mathscr{B}$. *treegraph* was chosen as it explicitly identifies internodes when generating a graph (Figure 5). Branches are identified as the longest path between a furcation and a tip and internodes are determined by identifying furcations through the network (Figure 5c). A taper function, similar to that applied in TreeQSM (Åkerblom, 2017), was applied to smooth variations in cylinder radius caused by residual point cloud noise. Where possible, branch tip widths were measured (see Section 2.5) and used to weight the polynomial functions that constrain cylinder radius; where this was not possible, tip width was determined by an unweighted taper function.

2.5 | Manual measurement of branches

To compare QSM modelled branch morphology and topology, a subset of branches (Table 1) were measured manually with a measuring tape and callipers (Bentley et al., 2013). For each branch, starting from the base (the point at which the branch was harvested), the length to the first node and distal radius was measured. Distal radius measurements were done with digital callipers where major and minor axes were measured at the base and below the furcation point. The internode was labelled and measurement moved onto the daughter internodes, this continued until all internodes had been measured; whether an internode was a tip (or broken) was also recorded. Parent–daughter internode connections were recorded to allow for a connected graph to be generated, analogous to a QSM. See Appendix S2 for more details on manual measurements.

2.6 | Number of branches scanned and measured

A total of 595 branches were scanned of which 15 were discarded from further analysis owing to data quality issues, for example, a branch moving between scans. The full architecture of 99 branches

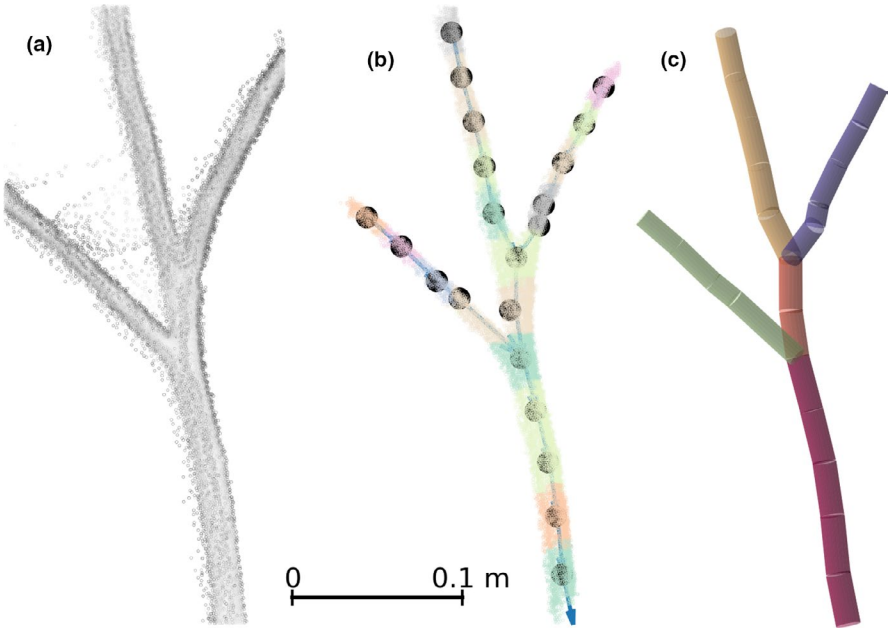

FIGURE 5 Examples of (a) an unfiltered branch point cloud ($\mathscr{B}'$), (b) a filtered branch point cloud ($\mathscr{B}$) and (c) the resulting QSM. Points are coloured by reflectance in (a). In (b), points are coloured by unique cluster $\mathscr{C}$, large points are cluster centroids that act as the start and end points of cylinders and arrows are the axis of the QSM cylinders determined by a graph where their direction is towards the base of the branch. The QSM in (c) is coloured by unique internode

were measured manually, 81 of which were scanned (16 branches had transcription errors which allowed for only partial comparison). A subset of tips (≤5 tips) of an additional 276 branches were also measured with callipers of which 266 were scanned. Example point clouds, QSM and reconstructions from manual measurements are illustrated in Figure 6.

3 | RESULTS AND DISCUSSION

Presented here is a method to reconstruct branch morphology and topology of harvested branches using a TLS-based workflow. Capturing this information across a single harvested tree, a single species across a plot or pan-tropically, for example, will allow for a greater understanding of branch architecture, for example, describing the major axes of architecture variation (Shenkin, Wilkes, et al., 2020). The workflow has been designed to give the best possible reconstruction of woody branch architecture, hence the requirement to remove leaves and scan in controlled environments. Therefore, the results (e.g. accuracy of reconstruction) may not be directly transferable to in-situ scanning of branches; however, scanning branches pre- and post-harvest or scanning harvested branches leaf-on and -off may provide a reference for in-situ reconstruction.

3.1 | Harvesting, scanning and manual measurement

Harvesting of branches is a laborious process requiring either large infrastructure or skilled personnel. Branch harvesting technique differed between location (Table 1) where climbers and the canopy crane resulted in the highest success rate while also allowing access to sunlit branches even in very tall trees (>60 m). Ground-based techniques were less successful leading to fewer (often larger) branches. Preparing branches for measurement, for example, removing leaves, can also be time-consuming; however, this can be combined with complementary leaf trait analysis.

Scanning branches was a far quicker process than manual measurement. Typically, 3–6 branches could be set-up and scanned in <30 min (10 min to set-up and 20 min to scan), whereas manual measurement required a two-person team per branch and a single branch may have taken >1 day to measure, that is, scan time is independent of branch size, whereas time to manually measure full architecture is not. Registering ~200 projects in RiScan Pro was time-consuming; however, once this was semi-automated (using the fiducial marker reflective dots as tie points) projects could be registered in ~15 min.

We recommend that a subsample of tip widths ($N \approx 5$) is measured with callipers to constrain the QSM taper function. This additional step improves the morphological representation of branches and leads to smaller errors in volume and surface area estimates (Figures 7 and 8).

3.2 | Post-processing of point clouds

Filtering $\mathscr{B}'$, as described in Section 2.4.1, removed ~ 64% ± 10% of points, where mean $|\mathscr{B}|$ was ~210,000 points. Fitting QSMs to $\mathscr{B}'$ without specifying tip width in the taper function significantly increases branch volume (bias = 171%) when compared to $\mathscr{B}$ with measured tip widths constraining the taper function (Figure 7a). Branch volume decreases when applying either filtering or tip-width correction; however, volumes are still larger than their fully processed counterparts where bias is 83% and 13%, respectively (Figure 7b,c). QSMs fitted to $\mathscr{B}'$ without specifying tip width decreases the number of internodes detected (bias = 1.8 internodes), particularly for shorter branches. As expected, specifying tip width

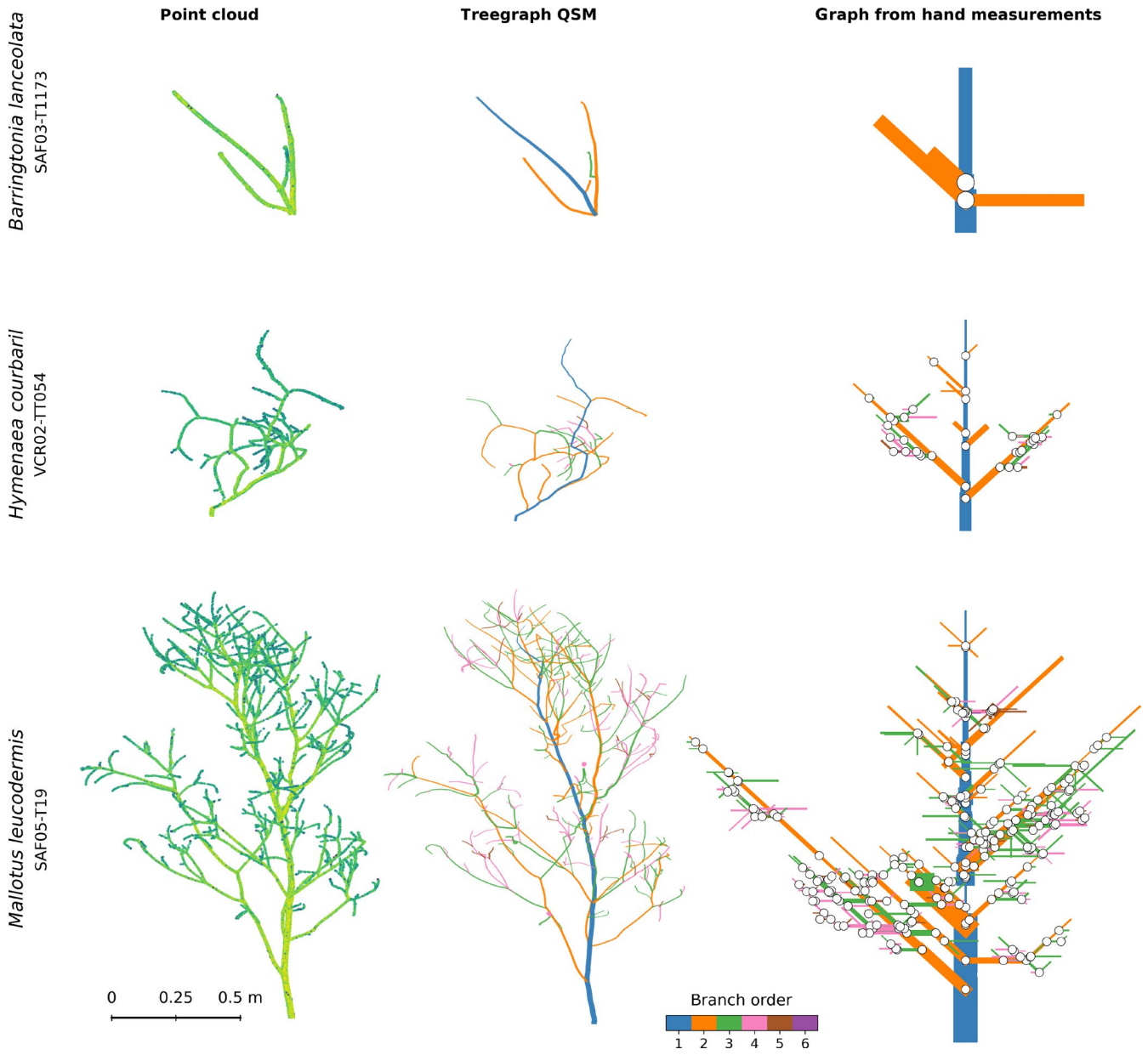

FIGURE 6 Examples of scanned branches where points are coloured by reflectance (left), computed quantitative structure models (QSM) (centre) and graphs derived from manual measurements (right)

has no impact on QSM topology derived from $\mathscr{B}'$ (Figure 7f). QSMs derived without a constrained taper function produces tend to overestimate smaller tip widths by 2–5 mm and underestimate tip width >3 mm (Figure 7g,i). There is an apparent good agreement between manually measured and QSM metrics derived from $\mathscr{B}$ (cf. Figure 8) suggesting that filtering and a constrained taper correction are necessary post-processing steps.

The model developed in Section 2.4.1 estimates branch diameter from ϕ_{max} where predicted and observed ϕ_{max} follow a similar trend of decreasing ϕ_{max} with decreasing branch radii (see Appendix S1). Observed ϕ_{max} is lower than the reflectance model would predict indicating that the branch surface is more attenuating of the laser pulse than predicted.

Computation of an accurate QSM requires a 'clean' underlying point cloud, sources of error that may precluded this are; scanner precision and accuracy (0.003 and 0.005 m, respectively; RIEGL Laser Measurement Systems GmbH, 2017), co-registration errors, to few points with which to construct a cylinder and noise, for example, edge points where $\mathbf{p}_{\phi} > \mathrm{E}[\phi_{min}]$. Even if a 'clean' point cloud is achieved, a number of external factors can lead to a poor QSM, for example the interior of highly ramified branches cannot be resolved owing to occlusion. Other sources of error that were not considered include ranging errors caused by waveform decomposition. Using an alternative decomposition function from a Gaussian (as onborad the RIEGL VZ-400), for example, skewed Gaussian (Zhu et al., 2018), may have yielded improved

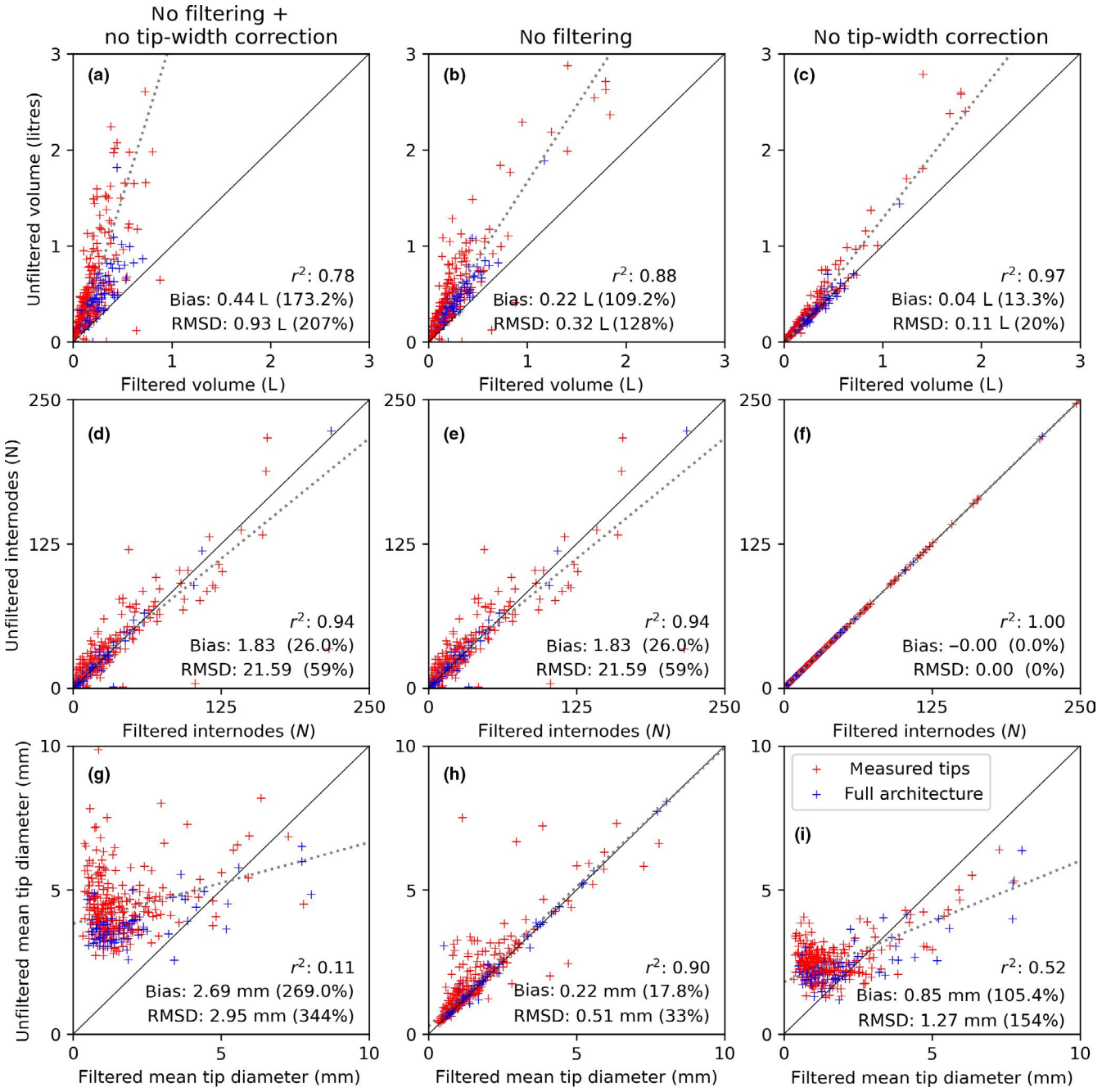

FIGURE 7 A comparison of QSM morphological (volume a–c and tip width g–i) and topological metrics (*N* internodes d–e) derived from unfiltered point clouds and without specifying tip width in the taper correction (left), unfiltered with a specified tip width (middle) and filtered point clouds without specifying tip width (right). All are compared to QSMs derived from filtered point clouds where tip width has been specified in the taper correction

results. However, full waveform data were not collected for this experiment.

3.3 | Branch architecture comparison

TLS-derived QSMs can characterise branch morphology and reconstruct topology accurately (Figures 6 and 8). Reconstructed total branch length is the most accurately reconstructed metric with a bias of 1.3% and RMSE of 10% when compared to manually measured branches (Figure 8a); an inability to reconstruct to the very tip may lead to a slight underestimate (Figure 8f). Regarding topology, TLS methods tend to overestimate the number of tips (bias = 0.03 tips, Figure 8d), particularly for smaller branches, but underestimate the number of internodes (bias = – 4.1 internodes, Figure 8f) due to the inability to resolve more ramified branching structures. Surface area (RMSE = 26%, bias = 9.9%, Figure 8c) and volume (RMSE = 43%, bias = 11.4%, Figure 8b) are overestimated by TLS methods owing to a tendency to

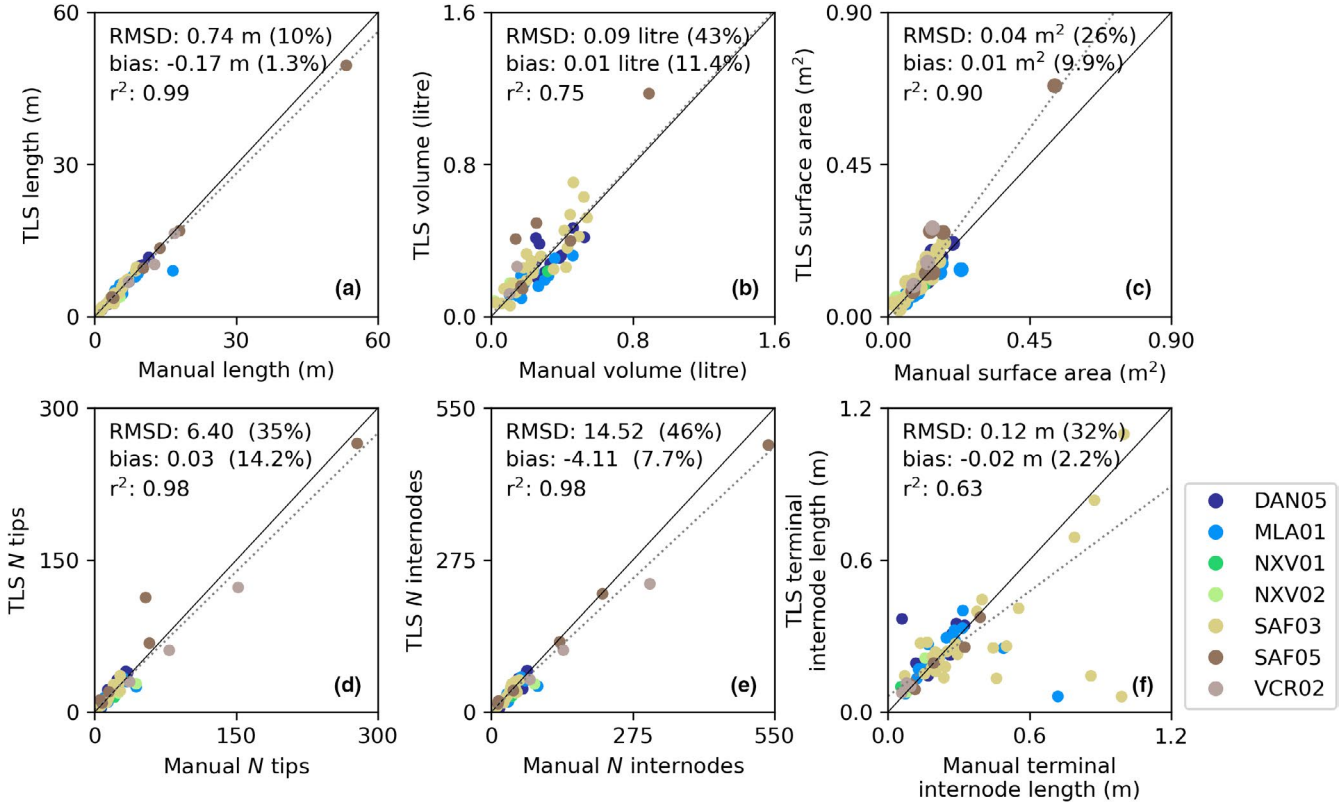

FIGURE 8 A comparison of terrestrial laser scanning (TLS)-derived and manually measured metrics of branch morphology and topology where panel (a) compares total branch length (b) total branch volume (c) total surface area (d) number (*N*) of branch tips (e) number of internodes and (f) mean length of terminal internode. Values in brackets are percentage RMSD and bias. The dashed line in each panel is a linear regression

overestimate branch radius even after taper correction. Inflation of radius towards the ends of the branches leads to a disproportionate overestimation in total volume, this is due to a compounding effect of many smaller internodes; radius inflation towards the base does not generally lead to an overestimation of total volume (Figure 9).

Although a concerted effort was made to remove noise from the branch point clouds, over inflation of branch radius was still prevalent. Taper functions can reduce overestimation, particularly towards branch tip; however, these are often data driven or require additional manual measurements (such as manual tip width measurements used here). More sophisticated taper functions with a physiological basis could improve volume and surface area estimates. Use of a cylinder as a geometric primitive may also not be most suitable candidate (although see Åkerblom et al., 2017). The mean ratio between major and minor axes as measured with callipers was 0.9, suggesting an elliptical primitive is more suitable. Using only the major axis when calculating volume results in a 6% overestimation of manually measured volume, compared to using major and minor axes. Furthermore, cylinder fitting to a point cloud cluster (i.e. $c \in C$) is naive in that a cylinder is fit to all points without regard for scan position (distance and viewing geometry) or a point quality weighting. A more intuitive cylinder fitting method may consider fitting iteratively to points from sequential scan positions or weighting points by an estimate of point quality. Artificial inflation of branch radius may have implications for whole tree volume and surface area estimates that are yet to be fully considered and should be investigated further.

A comparison radius and length scaling exponents generated from TLS and manual measurements are presented in Figure 10 (see Appendix S2 for methods used to calculate exponents). Both manually measured and TLS-derived radius exponents tended to be slightly greater than theoretical predictions, for example, West et al. (1999), whereas length exponents were less than predicted values. Similar results were presented by Bentley et al. (2013) and Lau et al. (2019) for branch level exponents measured across whole trees. Branches with a greater number of internodes (larger circles in Figure 10) tend towards the WBE scaling exponent value. Both TLS modelled and manually measured median length scaling exponents are <0 suggesting that, for the majority of branches, internode length increases towards branch tips. For branches with fewer internodes (smaller circles in Figure 10b), this could be caused by harvesting points not being located at a furcation.

It should be noted that metrics presented here were for comparison with manual measurements, that is, the suite of metrics were constrained by what could be measured manually in a reasonable time. For example, branching angle can be obtained by manual measurement but doing so would add a significant time burden; conversely, branch angle can be computed routinely with a TLS

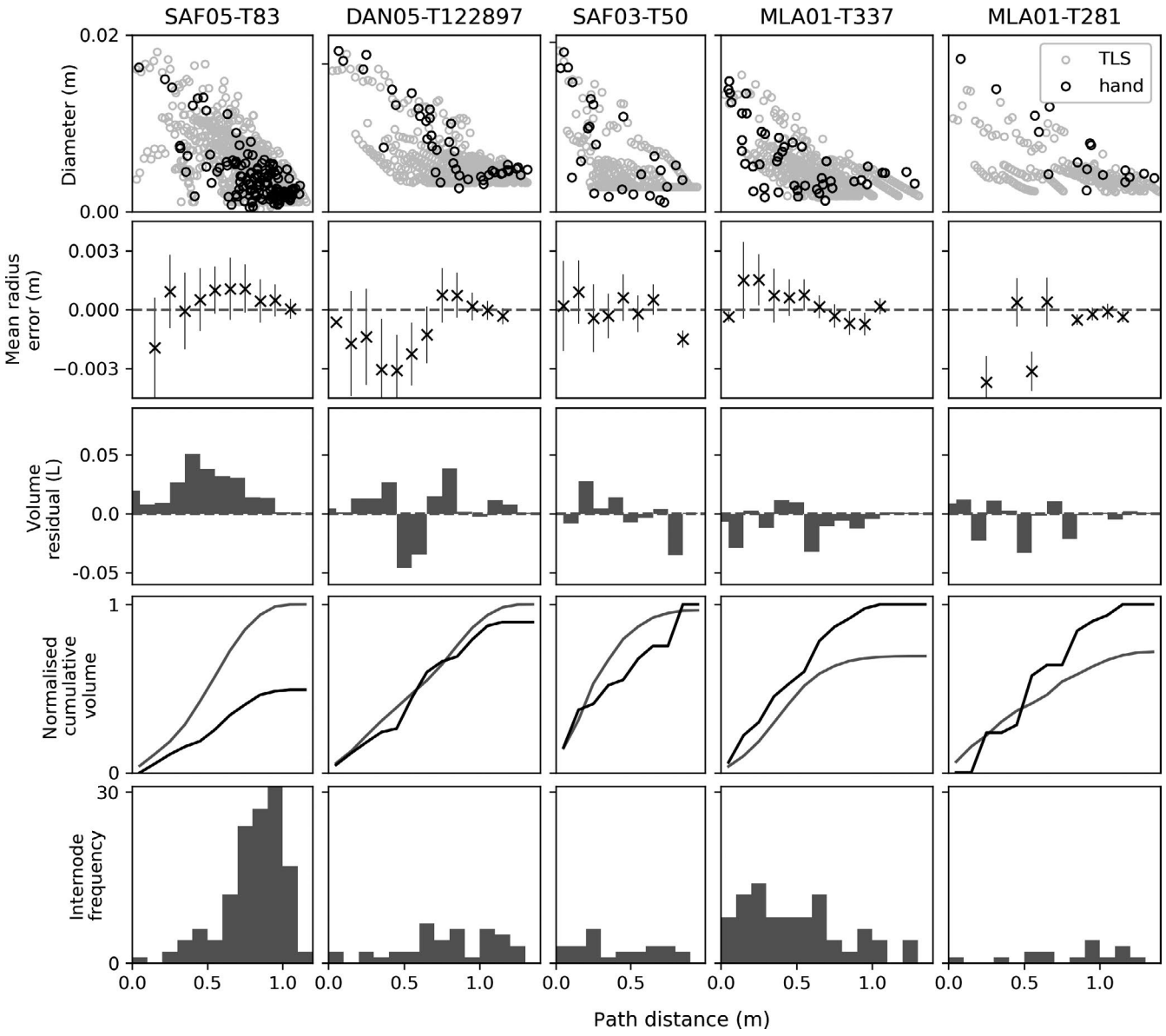

FIGURE 9 Analysis of radius measurements (top row), radius residuals (row 2), volume residual (row 3), cumulative volume (row 4) and internode frequency (bottom row) as a function of position along a branch. Five branches are shown where total branch volume is overestimated to underestimated ($l - r$) by terrestrial laser scanning (TLS) methods

workflow. A much larger suite of potential metrics could be generated from 3D measurement, examples include enclosing branches in alpha shapes which could then be used to explore space-filling theories related to branch length and leaf size (cf. Corners' Rule). Additionally, branch models could have further uses, for example in radiative transfer modelling to better characterise branch architecture when simulating forest scenes (Calders et al., 2018).

3.4 | Other scanning methods

Although the scanner used here was a high specification time-of-flight instrument, we suggest that the scanning and processing workflows are applicable to other TLS systems with only minor modifications. Phase shift laser scanners tend to have a smaller beam divergence (Abegg et al., 2020); however, they are often single return which may preclude scanning multiple branches at once. Other sensor methods may also become viable as technology improves (e.g. miniaturisation and ruggedness), in particular hand-held SfM and structured light systems where resolution is only limited by pixel size (Reichert et al., 2016; Wilkes et al., 2020).

4 | CONCLUSIONS

This paper presents a workflow to rapidly characterise the architecture (topology and morphology) of harvested branches using a TLS-based workflow. This involves branches being harvested and

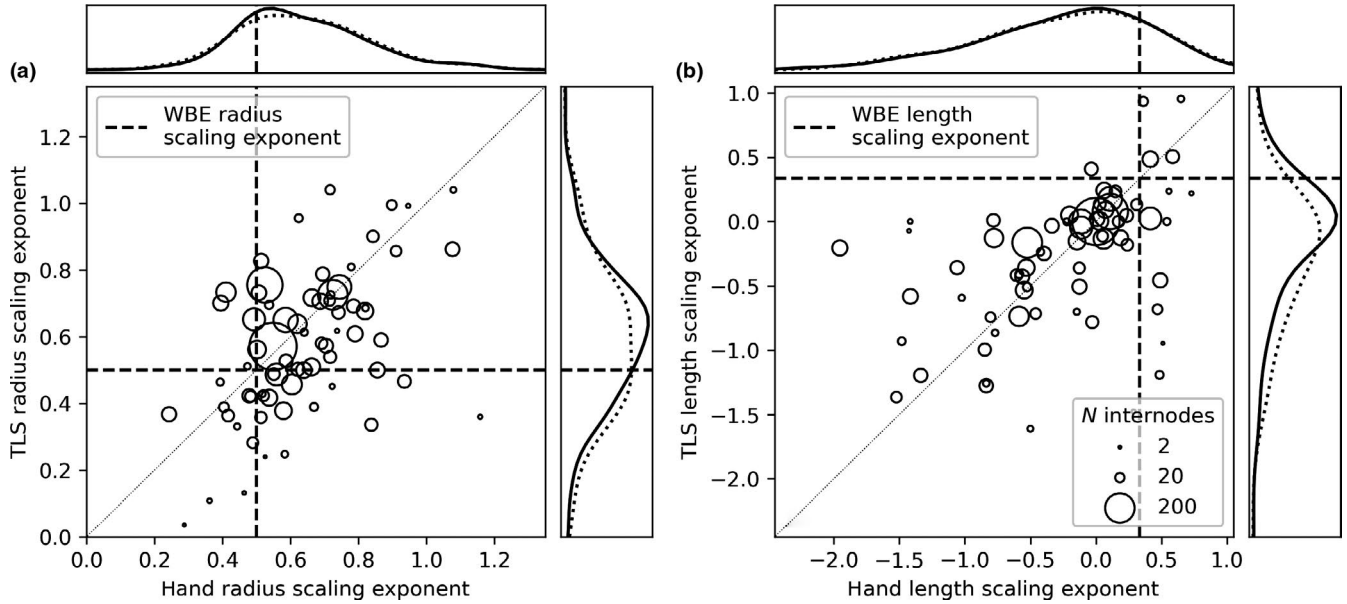

FIGURE 10 Mean branch-wise WBE scaling exponents calculated from terrestrial laser scanning (TLS) modelled and manual measurements for (a) radius and (b) length. Scatterplots compare values from manual and TLS measurements. Solid lines in subplots are branches that have been both scanned and manually measured, dashed lines represent all measured branches

stripped of leaves, scanned with TLS, post-processed to remove noise and finally parameterised with QSM methods. Post-processing requires a new dynamic reflectance filter to remove noise associated with partial interception of the laser footprint; such filtering may have application in whole tree TLS scanning and warrants further investigation. Metrics derived from scanned and modelled branches were correlated with manually measured analogues, demonstrating the method was successful in characterising branch architecture. Noise in point clouds towards branch tips caused an overestimation in tip width when compared to manual measurements. Constraining tip width in the QSM taper function with manual measurements improves the accuracy of morphological metrics. The suite of metrics used for comparison were limited by what could be manually measured; although not investigated here, new 3D measurements and metrics could be determined that could further enhance our understanding of branch architecture. Until sensor and platform technology improve to allow for accurate measurement and reconstruction of branches in-situ, it is suggested that workflows that use harvested branches remain the only option. However, the bottleneck for analysis is now harvesting branches and not architecture measurements; increased sample size and whole branch information provided by a TLS workflow would allow for a more comprehensive analysis of the 'missing link' between the leaves and larger diameter branches.

ACKNOWLEDGEMENTS

Branch samples were collected in Malaysia under permit JKM/MBS.1000-2/2 JLD.7 (87). This project was funded by the Natural Environment Research Council (NE/P011780/1) and we acknowledge capital support from NERC National Centre for Earth Observation (NCEO) and UCL Geography. Y.M. is supported by the Frank Jackson Foundation. We are hugely grateful to our project partners; Sabah Biodiversity Center, Chief Minister's Department Office of Internal Affairs & Research, Land & Survey Department, Sabah Forestry Department, the Maliau Basin and Danum Valley Management Committees, Forest Research Center (Sabah), Putri Ayu Asri, Suraya Afriyani Bahar, Sitti Mujur Channing Usman Duri, Dava Shini, Mohmmad fauzi, Subattyi ibang, Masdi Bin Asri, Fredino John, Almius Jupri, Jamiluddin Jami, Andy Burt, Lucas Cernusak, Alex Cheesman, Ana Palma, Lain Pardo, Michele Schiffer, Andrew Thompson and the Daintree Rainforest Observatory, Matt Bradford and CSIRO Atherton, the Jabalbina Yalanji Aboriginal Corporation, the Kuku Yalanji Traditional Owners, Ben Hur Marimon, Beatriz Marimon, Wesley Jonatar and Universidade do Estado de Mato Grosso (UNEMAT).

AUTHORS' CONTRIBUTIONS

Y.M., M.D. and L.P.B. conceived the project; P.W. and A.S. collected the data; P.W. and M.B.V. developed the software; P.W. conducted the analysis; all authors contributed to and approved the final manuscript.

CONFLICT OF INTEREST

The authors declare there are no conflicts of interest.

PEER REVIEW

The peer review history for this article is available at https://publons.com/publon/10.1111/2041-210X.13709.

DATA AVAILABILITY STATEMENT

The three branches presented in Figure 6 are available to download from Wilkes et al. (2021) as unfiltered and filtered point clouds, treegraph QSMs and manual measurements. Code to recreate workflows can be found at https://github.com/philwilkes/branch-extraction.

ORCID

Phil Wilkes http://orcid.org/0000-0001-6048-536X
Alexander Shenkin https://orcid.org/0000-0003-2358-9367
Mathias Disney https://orcid.org/0000-0002-2407-4026
Yadvinder Malhi https://orcid.org/0000-0002-3503-4783
Matheus Boni Vicari https://orcid.org/0000-0001-8841-4205

REFERENCES

Abegg, M., Boesch, R., Schaepman, M. E., & Morsdorf, F. (2020). Impact of beam diameter and scanning approach on point cloud quality of terrestrial laser scanning in forests. *IEEE Transactions on Geoscience and Remote Sensing*, 1–15. https://doi.org/10.1109/TGRS.2020.3037763

Åkerblom, M. (2017). Data from: Inversetampere/treeqsm: Initial release. *Zenodo*, https://doi.org/10.5281/zenodo.844626

Åkerblom, M., Raumonen, P., Mäkipää, R., & Kaasalainen, M. (2017). Automatic tree species recognition with quantitative structure models. *Remote Sensing of Environment*, *191*, 1–12.

Barthélémy, D., & Caraglio, Y. (2007). Plant architecture: A dynamic, multilevel and comprehensive approach to plant form, structure and ontogeny. *Annals of Botany*, *99*(3), 375–407. https://doi.org/10.1093/aob/mcl260

Bentley, L. P., James, C., Stegen, J. C., Savage, V. M., Smith, D. D., von Allmen, E. I., Sperry, J. S., Reich, P. B., & Enquist, B. J. (2013). An empirical assessment of tree branching networks and implications for plant allometric scaling models. *Ecology Letters*, *16*(8), 1069–1078.

Boni Vicari, M., Pisek, J., & Disney, M. I. (2019). New estimates of leaf angle distribution from terrestrial LiDAR: Comparison with measured and modelled estimates from nine broadleaf tree species. *Agricultural and Forest Meteorology*, *264*, 322–333.

Boni Vicari, M., & Wilkes, P. (2021). Data from: treegraph/source: Treegraph-branch-scanning. *Zenodo*, https://doi.org/10.5281/zenodo.5226212

Calders, K., Adams, J., Armston, J., Bartholomeus, H., Bauwens, S., Bentley, L. P., Chave, J., Danson, F. M., Demol, M., Disney, M., Gaulton, R., Krishna Moorthy, S. M., Levick, S. R., Saarinen, N., Schaaf, C., Stovall, A., Terryn, L., Wilkes, P., & Verbeeck, H. (2020). Terrestrial laser scanning in forest ecology: Expanding the horizon. *Remote Sensing of Environment*, *251*(September), 112102. https://doi.org/10.1016/j.rse.2020.112102

Calders, K., Burt, A., Origo, N., Disney, M. I., Nightingale, M., Raumonen, P., Akerblom, M., & Lewis, P. E. (2018). Virtual forests for radiative transfer modelling: Realistic forest stand reconstruction from terrestrial LiDAR. *Remote Sensing*, *10*, 1–15.

Calders, K., Newnham, G. J., Burt, A., Murphy, S., Raumonen, P., Herold, M., Culvenor, D. S., Avitabile, V., Disney, M. I., Armston, J. D., & Kaasalainen, M. (2015). Nondestructive estimates of above-ground biomass using terrestrial laser scanning. *Methods in Ecology and Evolution*, *6*(2), 198–208.

Calders, K., Phinn, S., Ferrari, R., Leon, J., Armston, J., Asner, G. P., & Disney, M. I. (2019). 3D imaging insights into forests and coral reefs. *Trends in Ecology & Evolution*, *35*(1), 6–9.

Chambers, J. Q., Tribuzy, E. S., Toledo, L. C., Crispim, B. F., Higuchi, N., Santos, J. D., Araújo, A. C., Kruijt, B., Nobre, A. D., & Trumbore, S. E. (2004). Respiration from a tropical forest ecosystem: Partitioning of sources and low carbon use efficiency. *Ecological Applications*, *14*(sp4), 72–88.

Cheng, Z.-L., Zhang, X.-P., & Chen, B.-Q. (2007). Simple reconstruction of tree branches from a single range image. *Journal of Computer Science and Technology*, *22*(6), 846–858.

del Campo-Sanchez, A., Moreno, M., Ballesteros, R., & Hernandez-Lopez, D. (2019). Geometric characterization of vines from 3D point clouds obtained with laser scanner systems. *Remote Sensing*, *11*(20), 2365.

Disney, M. (2019). Terrestrial LiDAR: A three-dimensional revolution in how we look at trees. *New Phytologist*, *222*(4), 1736–1741.

Disney, M. I., Boni Vicari, M., Burt, A., Calders, K., Lewis, S. L., Raumonen, P., & Wilkes, P. (2018). Weighing trees with lasers: Advances, challenges and opportunities. *Interface Focus*, *8*(2), 20170048.

Dutagaci, H., Rasti, P., Galopin, G., & Rousseau, D. (2020). ROSE-X: An annotated data set for evaluation of 3D plant organ segmentation methods. *Plant Methods*, *16*(1), 28.

Graham, A. W. (Ed.). (2006). *The CSIRO rainforest permanent plots of North Queensland: Site, structural, floristic and edaphic descriptions*. CSIRO and the Cooperative Research Centre for Tropical Rainforest Ecology and Management.

Iglhaut, J., Cabo, C., Puliti, S., Piermattei, L., O'Connor, J., & Rosette, J. (2019). Structure from motion photogrammetry in forestry: A review. *Current Forestry Reports*, *5*, 155–168.

Keightley, K. E., & Bawden, G. W. (2010). 3D volumetric modeling of grapevine biomass using Tripod LiDAR. *Computers and Electronics in Agriculture*, *74*(2), 305–312.

Lau, A., Bentley, L. P., Martius, C., Shenkin, A. F., Bartholomeus, H., Raumonen, P., Malhi, Y., Jackson, T., & Herold, M. (2018). Quantifying branch architecture of tropical trees using terrestrial LiDAR and 3D modelling. *Trees*, *32*(5), 1219–1231.

Lau, A., Martius, C., Bartholomeus, H. M., Shenkin, A. F., Jackson, T., Malhi, Y., Herold, M., & Bentley, L. P. (2019). Estimating architecture-based metabolic scaling exponents of tropical trees using terrestrial LiDAR and 3D modelling. *Forest Ecology and Management*, *439*(February), 132–145.

MacFarlane, D. W., & Kane, B. (2017). Neighbour effects on tree architecture: Functional trade-offs balancing crown competitiveness with wind resistance. *Functional Ecology*, *31*(8), 1624–1636.

Malhi, Y., Girardin, C., Metcalfe, D. B., Doughty, C. E., Aragão, L. E., Rifai, S. W., Oliveras, I., Shenkin, A., Aguirre-Gutiérrez, J., Dahlsjö, C. A., Riutta, T., Berenguer, E., Moore, S., Huasco, W. H., Salinas, N., da Costa, A. C. L., Bentley, L. P., Adu-Bredu, S., Marthews, T. R., … Phillips, O. L. (2021). The Global Ecosystems Monitoring network: Monitoring ecosystem productivity and carbon cycling across the tropics. *Biological Conservation*, *253*, 108889.

Malhi, Y., Jackson, T., Bentley, L. P., Lau, A., Shenkin, A., Herold, M., Calders, K., Bartholomeus, H., & Disney, M. I. (2018). New perspectives on the ecology of tree structure and tree communities through terrestrial laser scanning. *Interface Focus*, *8*(2), 20170052.

Martin-Ducup, O., Ploton, P., Barbier, N., Momo Takoudjou, S., Mofack, G., Kamdem, N. G., Fourcaud, T., Sonké, B., Couteron, P., & Pélissier, R. (2020). Terrestrial laser scanning reveals convergence of tree architecture with increasingly dominant crown canopy position. *Functional Ecology*, *34*(12), 2442–2452.

Moriondo, M., Leolini, L., Staglianò, N., Argenti, G., Trombi, G., Brilli, L., Dibari, C., Leolini, C., & Bindi, M. (2016). Use of digital images to disclose canopy architecture in olive tree. *Scientia Horticulturae*, *209*, 1–13.

Newnham, G. J., Armston, J. D., Muir, J., Goodwin, N. R., Tindall, D., Culvenor, D. S., Püschel, P., Nyström, M., & Johansen, K. (2012). *Evaluation of terrestrial laser scanners for measuring vegetation structure*. Technical report, manuscript ID: EP124571.

Nguyen, T. T., Slaughter, D. C., Max, N., Maloof, J. N., & Sinha, N. (2015). Structured light-based 3D reconstruction system for plants. *Sensors*, *15*(8), 18587–18612.

Rahman, A., Mo, C., & Cho, B.-K. (2017). 3-D image reconstruction techniques for plant and animal morphological analysis – A review. *Journal of Biosystems Engineering*, *42*(4), 339–349.

Raumonen, P., Kaasalainen, M., Åkerblom, M., Kaasalainen, S., Kaartinen, H., Vastaranta, M., Holopainen, M., Disney, M. I., & Lewis, P. E. (2013). Fast automatic precision tree models from terrestrial laser scanner data. *Remote Sensing*, *5*(2), 491–520.

Reichert, J., Schellenberg, J., Schubert, P., & Wilke, T. (2016). 3D scanning as a highly precise, reproducible, and minimally invasive method for surface area and volume measurements of scleractinian corals. *Limnology and Oceanography: Methods*, *14*(8), 518–526.

RIEGL Laser Measurement Systems GmbH. (2012). *LAS extrabytes implementation in RIEGL software*. Technical report.

RIEGL Laser Measurement Systems GmbH. (2017). *RIEGL RIEGL VZ-400 VZ-400*. Retrieved from www.riegl.com

RIEGL Laser Measurement Systems GmbH. (2019). *RiSCAN Pro Version 2.9.0*.

Sansoni, G., Trebeschi, M., & Docchio, F. (2009). State-of-the-art and applications of 3D imaging sensors in industry, cultural heritage, medicine, and criminal investigation. *Sensors*, *9*(1), 568–601. https://doi.org/10.3390/s90100568

Shenkin, A. F., Bentley, L. P., Oliveras, I., Salinas, N., Adu-Bredu, S., Marimon Junior, B. H., Marimon, B., Peprah, T., Choque, E. L., Trujillo Rodriguez, L., Clemente Arenas, E. R., Adonteng Booaheng, C., Seidu, J., Passos, F. B., Reis, S. M., Blonder, B., Silman, M., Enquist, B. J., Asner, G. P., & Malhi, Y. (2020). The influence of ecosystem and phylogeny on tropical tree crown size and shape. *Frontiers in Forests and Global Change*, *3*, 109.

Shenkin, A., Wilkes, P., Bentley, L., Disney, M., & Malhi, Y. (2020). The surface of trees: Architecture and global processes. In *3D Tree Models for Forest Dynamics*, 9th-10th Jan 2020, Helsinki, Finland.

Sillett, S. C., Van Pelt, R., Carroll, A. L., Kramer, R. D., Ambrose, A. R., & Trask, D. (2015). How do tree structure and old age affect growth potential of California redwoods? *Ecological Monographs*, *85*(2), 181–212.

Smith, D. D., Sperry, J. S., Enquist, B. J., Savage, V. M., Mcculloh, K. A., & Bentley, L. P. (2014). Deviation from symmetrically self-similar branching in trees predicts altered hydraulics, mechanics, light interception and metabolic scaling. *New Phytologist*, *201*(1), 217–229.

Valladares, F., & Lo Niinemets, U. Â. (2007). The architecture of plant crowns: From design rules to light capture and performance. In F. Pugnaire & F. Valladares (Eds.), *Functional plant ecology* (pp. 101–139). Taylor and Francis.

West, G. B., Brown, J. H., & Enquist, B. J. (1999). A general model for the structure and allometry of plant vascular systems. *Nature*, *400*(6745), 664–667.

Wilkes, P. (2021). *qrDAR*. Retrieved from https://github.com/philwilkes/qrdar

Wilkes, P., Lau, A., Disney, M. I., Calders, K., Burt, A., de Tanago, G., Menaca, J., Bartholomeus, H. M., Brede, B., Herold, M., de Tanago, J. G., Bartholomeus, H. M., Brede, B., & Herold, M. (2017). Data acquisition considerations for terrestrial laser scanning of forest plots. *Remote Sensing of Environment*, *196*, 140–153.

Wilkes, P., Shenkin, A., Disney, M., Mahli, Y., & Bentley, L. P. (2020). Terrestrial LiDAR and photogrammetry for rapid characterisation of fine scale branch structure. In *3D tree models for forest dynamics*. 9th-10th Jan 2020. Helsinki, Finland.

Wilkes, P., Shenkin, A., Disney, M., Malhi, Y., Bentley, L. P., & Vicari, M. B. (2021). Data from: Terrestrial laser scanning to reconstruct branch architecture from harvested branches. *Zenodo*, https://doi.org/10.5281/zenodo.4555536

Zhu, X., Skidmore, A. K., Wang, T., Liu, J., Darvishzadeh, R., Shi, Y., Premier, J., & Heurich, M. (2018). Improving leaf area index (LAI) estimation by correcting for clumping and woody effects using terrestrial laser scanning. *Agricultural and Forest Meteorology*, *263*, 276–286.

SUPPORTING INFORMATION

Additional supporting information may be found online in the Supporting Information section.

How to cite this article: Wilkes, P., Shenkin, A., Disney, M., Malhi, Y., Bentley, L. P., & Vicari, M. B. (2021). Terrestrial laser scanning to reconstruct branch architecture from harvested branches. *Methods in Ecology and Evolution*, 00, 1–14. https://doi.org/10.1111/2041-210X.13709